

# Multiscale Data-driven Seismic Full-waveform Inversion with Field Data Study

Shihang Feng<sup>1,\*</sup>, Youzuo Lin<sup>1,\*</sup> and Brendt Wohlberg<sup>2</sup>

**Abstract**—Seismic full-waveform inversion (FWI), which applies iterative methods to estimate high-resolution subsurface detail from seismograms, is a powerful imaging technique in exploration geophysics. In recent years the computational cost of FWI has grown exponentially due to the increasing size and resolution of seismic data. Moreover, it is a non-convex problem, and can become stuck in a local minima due to the limited accuracy of the initial velocity maps, the absence of low frequencies in the measurements, the presence of noise, and the approximate modeling of the wave-physics complexity. To overcome these computational issues, we develop a multiscale data-driven FWI method based on the fully convolutional network (FCN). In preparing the training data, we first develop a real-time style transform method to create a large set of physically realistic subsurface velocity maps from natural images. We then develop two convolutional neural networks with encoder-decoder structure to reconstruct the low- and high-frequency components of the subsurface velocity maps, respectively. To validate the performance of our new data-driven inversion method and the effectiveness of the synthesized training set, we compare it with conventional physics-based waveform inversion approaches using both synthetic and field data. These numerical results demonstrate that, once our model is fully trained, it can significantly reduce the computation time, and yield more accurate subsurface velocity map in comparison with conventional FWI.

**Index Terms**—Seismic Full-waveform Inversion, Scientific Deep Learning, Style Transfer, Multiscale Analysis, Data Augmentation

## I. INTRODUCTION

Accurately and efficiently characterizing subsurface geology is crucial for various applications, such as energy exploration, civil infrastructure, groundwater contamination and remediation, etc. The standard approach to obtaining such a characterization is via computational seismic imaging, which involves reconstructing an image of subsurface structures from measurements of natural or artificially produced seismic waves. There are two primary ways of solving this problem, depending on the complexity of the forward modeling. The simpler approach is via travel-time inversion [1], which has a linear forward operator, but provides results of inferior accuracy and resolution. Full-waveform inversion (FWI) techniques [2] provide superior solutions by modeling the wave propagation in the subsurface, but the forward operator is non-linear and computationally expensive. The problem of FWI is ill-posed, without a unique solution [2], making a prior model of the

solution space essential. Since regularized inversion methods solved via iterative optimization techniques need to apply the forward operator hundreds or thousands of times, these solutions are very computationally expensive. Furthermore, with the explosive growth in data volumes due to the development of seismic acquisition technology [3], solving FWI problems for large-scale data set becomes computationally prohibitive or even infeasible.

Inspired by recent successes in applying deep learning to computer vision and medical problems, deep-learning-based data-driven methods had been applied to FWI problems. Several encoder-decoder networks have been developed to reconstruct the subsurface structure from seismic data [4, 5, 6, 7]. Those deep-learning models are end-to-end, meaning that they use the seismic waveform data as the input and directly output its corresponding subsurface structure. Once those models are fully trained, the inversion procedure is extremely computationally efficient. However, a significant weakness of these data-driven methods is their weak generalization ability, which hinders the wide application of data-driven seismic imaging approaches to field data [7].

Weak generalization is a common challenge facing all deep-learning applications. It means the predictive models trained in a specific dataset cannot perform well when applying to an out-of-distribution dataset. To improve the generalization ability, novel models have been developed to incorporate physics laws and prior information (such as geometric rules, symmetries or other relevant constraints) into the deep learning models [8, 9]. Alternatively, the robustness and generalization ability of deep learning models can be improved by acquiring more labeled data. However, neither of these is straightforward for seismic imaging. The current state-of-the-art physics-based (theory-guided) FWI approaches can provide limited constraints with respect to the governing physics. Furthermore, it can be extremely difficult and expensive to collect real subsurface structure maps and their corresponding seismic measurements, which results in training sets with limited representativeness. To overcome the weak generalization issue, we explore the possibility of enriching the training set and incorporating critical physics phenomena in our predictive model.

A high quality training dataset with sufficient representativeness is the foundation for obtaining a robust predictive model [10]. Particularly for seismic imaging, a training set with high representativeness should not only account for geological variability but also be compatible with domain knowledge and intrinsic physics rules. However, there has been surprisingly little work to address the lack of labeled data in the exploration geophysics community. Ovcharenko et. al [11]

<sup>1</sup>: Earth and Environmental Sciences Division, Los Alamos National Laboratory, Los Alamos, NM, 87544 USA.

<sup>2</sup>: Theoretical Division, Los Alamos National Laboratory, Los Alamos, NM, 87544 USA.

\*Correspondence to: S. Feng (shihang@lanl.gov) and Y. Lin (ylin@lanl.gov).

developed a set of subsurface structure maps using customized subsurface random model generators. Their method strongly relies on domain knowledge to generate the content images, which in turn significantly limits the variability of the training set. Wu et. al [12] designed a workflow to automatically build subsurface structure with folding and faulting features. Their method relies on the initial layer-like structure, therefore, producing unsatisfactory results when applying to different sites. To address this dilemma and improve the weak generalization ability of data-driven inversion, we develop a new data generation technique to incorporate critical physics information and enrich data representativeness. Our idea is inspired by the artistic style transfer problems from computer vision community, the goal of which is to transfer the art style of one painting to another image by minimizing the style loss and the content loss based on features extracted from a pre-trained convolutional neural network (CNN) [13, 14, 15]. Those tools therefore provide us with means to bridge images from two different physical domains. Specifically, subsurface structure maps represent the geophysical properties in 2D, which can be also viewed as images of a certain physical property. Built on existing style transfer approaches, our method converts a large volume of existing natural images into subsurface structure maps with pre-determined geologic styles. In such a manner, our method can generate a large number of physically realistic subsurface velocity maps with sufficient variability. That in turn not only helps our data-driven models to learn the governing physics (forward model) of the problem through training, but also yields high generalization ability due to the richness of the data representativeness. Among various existing style transfer algorithms [13, 14, 15], we employ the one developed by Johnson et al. [13] due to its efficiency in solving the optimization. In particular, its feed-forward network can be run in real-time after training, so that it is feasible to generate numerous realistic art images efficiently.

Incorporation of critical physics into neural network structures also plays an important role in improving the robustness of predictive models [8, 16, 17, 18]. Unlike conventional FWI, where the relationship between seismic data and velocity map is governed by the wave-equation, data-driven FWI methods learn a correspondence from seismic data directly to subsurface structure. The governing physics of the forward modeling is represented implicitly in the training dataset [19]. On the other hand, the propagation of seismic wave is a complex physical phenomenon, which consists of different waves, such as reflection waves, transmission waves and direct waves, etc. Each of them follows different wavepaths and propagation mechanisms. To account for the complex physics and better explain the various wave phenomena, we develop a multiscale inversion strategy. It is worthwhile to mention that multiscale techniques have been widely used in convectional physics-based FWI approaches [20, 21, 22] to handle different waves and preventing local minima. With this strategy incorporated, our new data-driven FWI is able to separately invert transmission and reflection waves in the seismic data. Particularly, the predicted results from the low-frequency components can be used as the initial guess for the high-resolution inversion, which significantly improves the overall inversion accuracy.

To combine all those computational modules that we develop, we first train a feed-forward style transfer network to generate numerous physically realistic velocity maps. Those velocity maps and their corresponding seismic data are then utilized to train our multiscale data-driven FWI networks, called “Multiscale InversionNet”. Once the network is fully trained, the model can effectively and efficiently invert the seismic data to obtain velocity maps.

This paper is organized in six sections. After the introduction in the first section, the second section presents the theories with image style transfer and seismic full-waveform inversion. Our new proposed methodologies of building realistic velocity model and multiscale InversionNet are introduced in the third section. The fourth section shows the numerical results with both synthetic and field data. A discussion of our Multiscale InversionNet is presented in the fifth section. Finally, the conclusion is given in the last section.

## II. THEORY

### A. Seismic Full-waveform Inversion

The forward model of our problem is the acoustic-wave equation, which is given by

$$\nabla^2 p(\mathbf{r}, t) - \frac{1}{c^2(\mathbf{r})} \frac{\partial^2 p(\mathbf{r}, t)}{\partial t^2} = s(\mathbf{r}, t) \quad (1)$$

where  $c(\mathbf{r})$  is the velocity at spatial location  $\mathbf{r}$ ,  $\nabla^2 = \left( \frac{\partial^2}{\partial x^2} + \frac{\partial^2}{\partial z^2} \right)$  is the Laplacian operator in Cartesian coordinates,  $s(\mathbf{r}, t)$  is the source term,  $p(\mathbf{r}, t)$  is the pressure wavefield, and  $t$  represents time. To simplify the expression, we rewrite the forward modeling problems in Eq. (1) as

$$\mathbf{d} = f(\mathbf{m}), \quad (2)$$

where  $\mathbf{d}$  is the pressure wavefield for the acoustic case,  $f$  is the forward acoustic-wave modeling operator, and  $\mathbf{m}$  is the model parameter vector, including the density and compressional- (P-) velocities.

1) *Physics-based Full-waveform Inversion*: In the physics-based full-waveform inversion, the objective function is

$$l_{\text{FWI}} = \frac{1}{2} \sum_{s,g} \|\mathbf{d}_{s,g}^{\text{pre}} - \mathbf{d}_{s,g}^{\text{true}}\|^2, \quad (3)$$

where  $\mathbf{d}_{s,g}^{\text{pre}}$  and  $\mathbf{d}_{s,g}^{\text{true}}$  are the predicted and observed data at the locations of receivers  $g$  and sources  $s$ . The model is gradually reconstructed using gradient-based optimization methods to calculate  $f^{-1}$ , which are computationally expensive.

2) *Data-driven Full-waveform Inversion*: Unlike the physics-based full-waveform inversion, which calculates the inversion using an iterative method, data-driven seismic inversion obtains an approximation of  $f^{-1}$  by training an encoder-decoder network [4]. It achieves the data-driven FWI by regressing seismic data  $\mathbf{d}$  to velocity map  $\mathbf{m}$  directly. More details of data-driven inversion approaches can be found in our previous work [4].

### B. Image Style Transfer

Image style transfer can be defined as finding a composite image  $y$  whose style is similar to a style image  $y_s$  and content

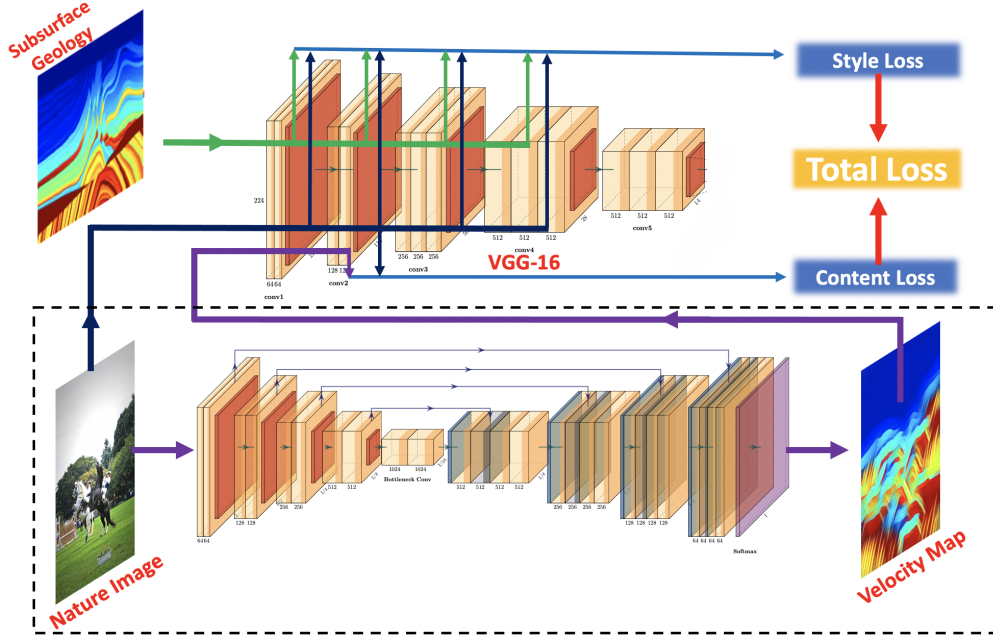


Fig. 1: The style transform system overview. The image transform network is trained to transform natural image into a realistically velocity perturbation. A pre-trained VGG-16 network is used to calculate the style and content loss, it is fixed during the training procedure.

is similar to a content image  $y_c$ . Two images are similar in style if their low-level features extracted by a trained classifier have similar Gram matrix  $G_j(x)_{mn}$  [14, 15]

$$G_j(x)_{mn} = \sum_p \phi_j(x)_{mp} \phi_j(x)_{np}, \quad (4)$$

where  $\phi_j(x)$  is the activations at the  $j$ th layer of the network  $\phi$  for the input  $x$  and the Gram matrix is the inner product between the vectorized feature maps in layer  $j$ . The style loss is defined as

$$l_{\text{style}} = \sum_{j \in S} \frac{1}{U_j} \|G_j(y) - G_j(y_s)\|^2, \quad (5)$$

where  $S$  is a set of layers used in style reconstruction,  $U_j$  is the total number of units in layer  $j$  and  $y_s$  is the style image and  $y$  is the composite image. Two images are similar in content if their high-level features extracted by a trained classifier are close. The content loss is defined as below

$$l_{\text{content}} = \sum_{j \in C} \frac{1}{U_j} \|\phi_j(y) - \phi_j(y_c)\|^2, \quad (6)$$

where  $C$  is a set of layers used in content reconstruction and  $y_c$  is the content image. The real-time style transfer system is shown in Figure 1, where the right side is the calculation of the loss function of the network. The overall loss is defined as

$$l_{\text{trans}} = \alpha_{\text{style}} l_{\text{style}} + \alpha_{\text{content}} l_{\text{content}}, \quad (7)$$

where  $\alpha_{\text{style}}$  and  $\alpha_{\text{content}}$  are the weights for style and content reconstruction. By defining the loss function as Eq. (7), the image transform feed-forward networks are trained to solve the optimization problem.

### III. METHODOLOGY

#### A. Building Physically Realistic Velocity Maps

The current data-driven seismic FWI approaches rely heavily on the pre-generated simulations. However, the unavoidable discrepancy between simulations and field data severely limits the representiveness of the training dataset, which hinders its application in field data. In order to bridge the gap between simulation and field data, we expect a high-quality training dataset should consist of a large volume of subsurface velocity maps with sufficient variability in order to represent the complex geology in various scenarios. To our best knowledge, there is no such a dataset existing for training seismic FWI problems. To overcome this data challenge, we develop a new domain-agnostic data generation approach that is capable of synthesizing a large volume of physically realistic subsurface velocity maps efficiently. Specifically, our approach is built on natural image dataset (COCO dataset [23] in this work), taking advantage of its large sample size, high image quality, and varying visual perception. We develop a domain adaptation technique to transfer natural images from COCO dataset to subsurface velocity maps. Our data-generation technique can produce a large number of synthetic subsurface velocity maps that is consistent with the subject matter expertise.

Inspired by the work of Johnson et al. [13], we design a neural network to generate subsurface velocity map as shown in Figure 1. The inputs of our network include the content natural image and the style image. We will convert the content natural image into a subsurface structure map, which contains the geologic features learned from the style image. Particularly, in this network architecture, we use the relu1\_2, relu2\_2, relu3\_3 and relu4\_3 layers in VGG16

network [24] for style reconstruction and the relu2\_2 for content reconstruction.

The results with different style weights are shown in Figure 2. As the style weight increases, the composite image contains more geological features and becomes more similar to the subsurface structure.

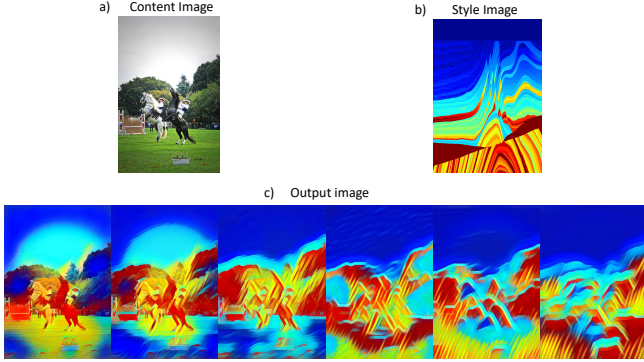


Fig. 2: a) Content image, b) style image and c)-h) output style transfer images with style weight = 1e9, 3e9, 5e9, 8e9, 1e10 and 5e10.

The color distributions in natural images are different from the velocity distributions in the subsurface structure. Since the composite images obtain their content from the natural images, there are clear differences between the composite images and the real subsurface velocity maps.

To mimic the real subsurface velocity maps, the composite image obtained from style transfer is converted to a single-channel gray-scale image and normalized to a velocity perturbation map. Next, a 1D velocity map with linearly increasing value is utilized as the background velocity. The composite velocity map as shown in Figure 3 is obtained by combining these two maps using following equation:

$$v_{com} = \beta_{pert} v_{pert} + (1 - \beta_{pert}) v_{back}, \quad (8)$$

where  $v_{com}$ ,  $v_{pert}$  and  $v_{back}$  are the composite velocity map, the velocity perturbation map and the background velocity map, respectively.  $0.1 < \beta_{pert} < 0.3$  is the weight of the velocity perturbation map. We therefore synthesize a physically meaning subsurface velocity map, which inherits geological features from the style image.

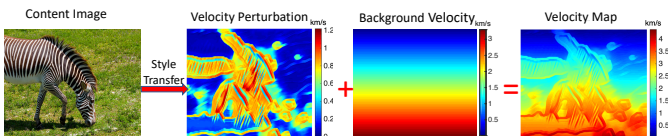


Fig. 3: The workflow of creating realistic velocity maps. The content images are transferred to velocity perturbation map using the trained image transform network. Then 1D linear-increased background velocity is added to compose realistic velocity maps

## B. Multiscale InversionNet

The kinematic of seismic wave propagation is complex, which make the inversion of the full-waveform inversion a complicated problem. The multiscale methodology is able to break the complex inversion into a series of simply inversion procedures. Such methodology has been applied in the physics-based full-waveform inversion to mitigate the local minimal problem by proceeding the seismic data from low to high frequency. In this section, we will study how to apply such a multiscale idea in the data-driven full-waveform inversion.

Built on our previous work of InversionNet [4], our Multiscale InversionNet consists two modules: a low-resolution InversionNet and a high-resolution InversionNet. Particularly, the low-resolution InversionNet is used to invert the low-frequency components of the velocity maps, and the high-resolution InversionNet is applied to reconstruct the high-frequency components of the velocity maps.

1) *Low-resolution InversionNet*: To invert the low-frequency component of the velocity map, we design the architecture of the low-resolution InversionNet as shown in Figure 4. We choose the  $\ell_2$  loss function as our optimality criterion:

$$l_{inv\_low} = \frac{1}{N} \sum_{i=1}^N \|\mathbf{m}_i^{\text{pre\_low}} - \mathbf{m}_i^{\text{true\_low}}\|^2, \quad (9)$$

where  $\mathbf{m}_i^{\text{pre\_low}}$  and  $\mathbf{m}_i^{\text{true\_low}}$  are the low-resolution velocity map predicted by network and the ground truth with  $i$ th training sample, respectively. The variable  $N$  is the total number of the training samples. For a more detailed discussion of loss function selection, please refer to our earlier work [4].

2) *High-resolution InversionNet*: The purpose of our high-resolution InversionNet is to refine the low-frequency velocity component learned via the low-resolution InversionNet by accounting for reflection wave from the data. To achieve this, we design a different encoder-decoder network architecture as shown in Figure 5. The encoder consists of two parts: a map section and a data section. The map section, as shown in blue box (Figure 5), is an U-net [25] like encoder that incorporates the low-frequency information of the velocity map into the network. The input is the predicted low-resolution velocity map from low-resolution InversionNet. The second section, as shown in red box (Figure 5), is an encoder that adds data information in the network. The input is the data residual calculated as

$$\mathbf{d}_i^{\text{diff}} = \mathbf{d}_i^{\text{pre}} - \mathbf{d}_i^{\text{true}}, \quad (10)$$

where  $\mathbf{d}_i^{\text{pre}}$  and  $\mathbf{d}_i^{\text{true}}$  are the predicted data generated from low-resolution velocity map and the observed data with  $i$ th training sample, respectively.

The loss function can be define as a  $\ell_2$  loss function,

$$l_{inv\_high} = \frac{1}{N} \sum_{i=1}^N \|\mathbf{m}_i^{\text{pre\_high}} - \mathbf{m}_i^{\text{true\_high}}\|_2^2, \quad (11)$$



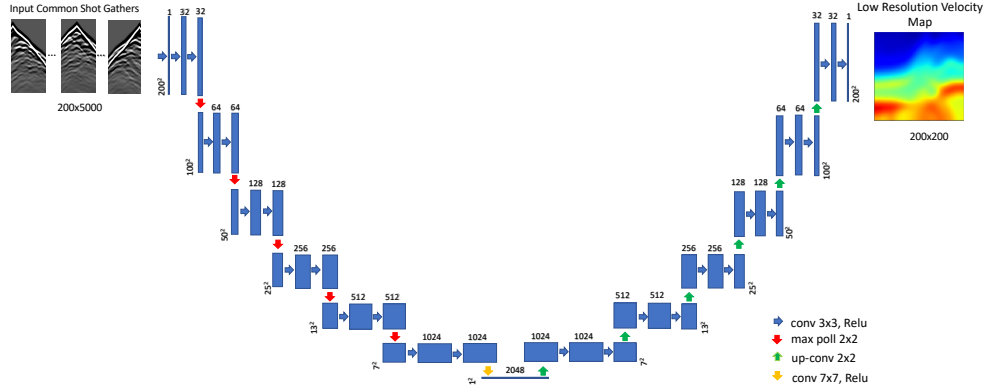


Fig. 4: An illustration of Low Resolution InversionNet.

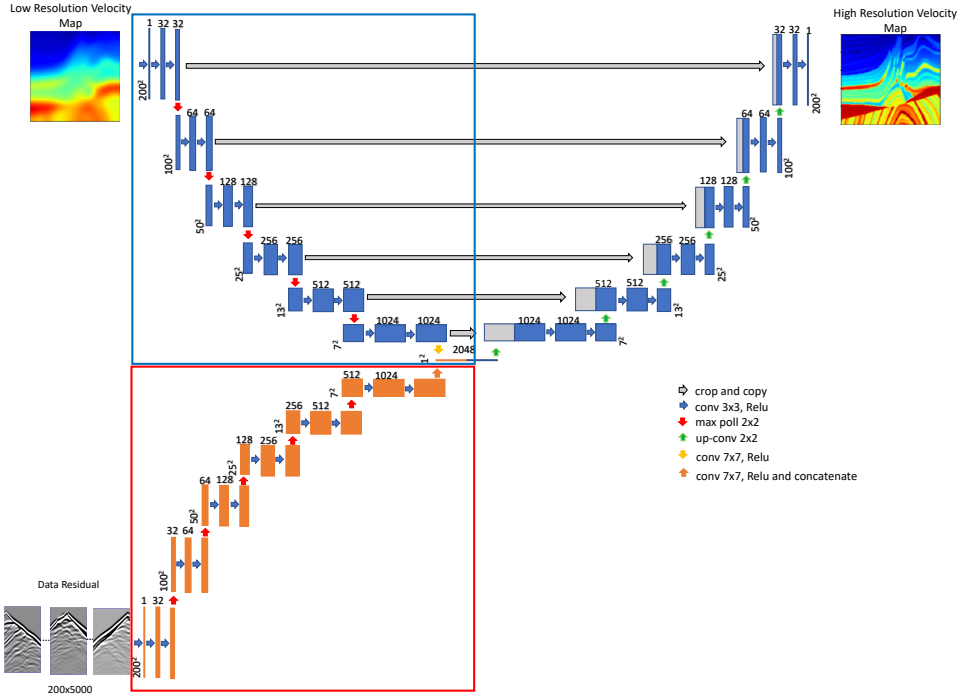


Fig. 5: An illustration of High Resolution InversionNet.

or a  $\ell_1$  loss function

$$l_{inv\_high} = \frac{1}{N} \sum_{i=1}^N \|\mathbf{m}_i^{\text{pre\_high}} - \mathbf{m}_i^{\text{true\_high}}\|_1, \quad (12)$$

where  $\mathbf{m}_i^{\text{pre\_high}}$  and  $\mathbf{m}_i^{\text{true\_high}}$  are the low-resolution velocity map predicted by network and the ground truth with  $i$ th training sample, respectively.

3) *Training Strategy*: Training both the map- and data-sections in the high-resolution InversionNet as shown in Figure 5 can be technically challenging due to the different physical properties of inputs. A straight-forward training strategy to train our high-resolution InversionNet simultaneously can lead to an unbalanced convergence, meaning that one section of the network would dominate the training procedure over the other section. To mitigate this issue, we design a two-step

alternative training scheme:

- i. Fix the parameters in the red box and update the parameters in the blue box and the decoder so that the low-frequency information of the velocity map can be leveraged in the learning process.
- ii. Fix the parameters in the blue box and update the parameters in the red box and the decoder. Similar with the conventional FWI, the data residual are used to update the velocity map to reconstruct the high frequency information.

We alternatively iterate the training procedure between Steps 1 and 2. Once the training is completed, our high-resolution InversionNet can be used to infer subsurface velocity map with an initial guess from the low-resolution InversionNet and the data differences.

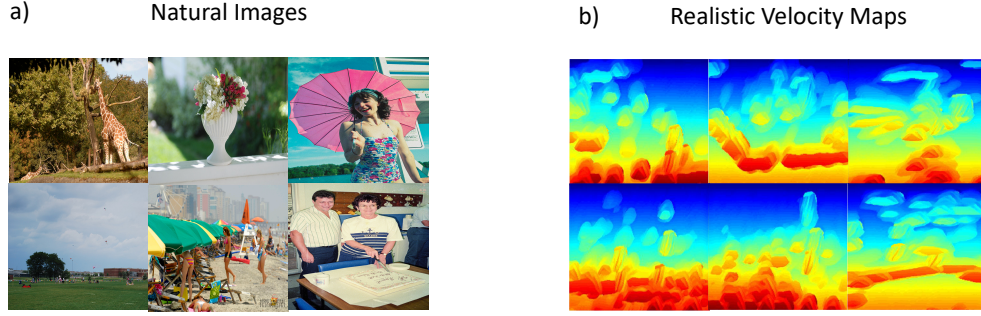


Fig. 6: a) Natural images from COCO dataset [23] and b) the corresponding synthesized physically realistic subsurface velocity maps.

### C. Inversion Procedure

To summarize, we provide the workflow for the implementation of our Multiscale InversionNet as the following 3 steps:

- i. **Data Preparation:** Apply style transfer on the natural images to generated velocity perturbations. Combine the generated velocity perturbations with the 1D velocity maps to composite realistic velocity maps.
- ii. **Low-resolution Inversion:** Smooth the composite realistic velocity maps and generate their corresponding seismic data using forward modeling. Use the smoothed velocity maps and their seismic data to train the low-resolution InversionNet. Then apply the trained low-resolution InversionNet on the test data.
- iii. **High-resolution Inversion:** Generate the seismic data with the high-resolution realistic velocity maps. Use the high-resolution velocity maps and seismic data to train the high-resolution InversionNet. Then apply the trained high-resolution InversionNet on the test data.

## IV. RESULTS

### A. Synthetic Tests

1) *Data Preparation:* We first conduct a synthetic test to demonstrate the performance of our methodology. 67,000 natural images from the COCO dataset [23] are used as the content images and the Marmousi [26] velocity map as the style image to construct the physically realistic subsurface velocity maps. The geometry of the Marmousi velocity map is based on a profile of the North Quenguela through the Cuanza basin [27]. The Marmousi model was built to resemble a continental drift geological setting. It contains many typical geological structures, such as reflectors, steep dips, and strong velocity variations in both the lateral and the vertical direction [26]. Figure 6 shows the natural images from the COCO data set and the generated realistic velocity maps using our approach (as illustrated in Figure 1). In order to obtain velocity maps with different resolutions, the realistic velocity maps are smoothed by a Gaussian filter with random standard deviation from 6 to 10 as low-resolution velocity maps and with random deviation from 0 to 5 as high-resolution velocity maps.

These realistic subsurface velocity maps have been reshaped to the same size of 2 km in both  $x$  and  $z$  directions with a grid

spacing of 10 m. Ten sources are located on the surface with a spacing of 200 m, and the traces are recorded by 200 receivers spaced at an interval of 10 m. The source wavelet is a Ricker wavelet with a peak frequency of 15 Hz [28]. We choose a Ricker wavelet as the source function to generate seismic waves due to its empirical success in processing seismic field data [29]. The seismic data are generated using the finite-difference method with the acoustic wave equation [30].

To validate the performance of our approach, we test our network on both in-distribution and out-of-distribution datasets. In particular, the in-distribution datasets are randomly selected from our test data (as shown in Figures 7(a) and (d)). Two out-of-distribution datasets, i.e., Marmousi and Overthrust [31] velocity maps, are selected for testing due to their popularity (as shown in Figures 7(b) and (e), and Figures 7(c) and (f), respectively). We smooth the Marmousi and Overthrust velocity maps by a Gaussian filter with random standard deviation from 0 to 10 to validate if the low-resolution inversion can extract a low-resolution velocity map even the data generated by velocity maps with different resolution.

2) *Low-resolution Inversion:* Similar to conventional multiscale full waveform inversion, the first step is to construct the low-frequency component of the velocity map from the data. To train the low-resolution InversionNet, 64,000 pairs of low-resolution velocity maps and their corresponding seismic measurements are used. An additional 3,000 pairs are used for testing. Since the velocity maps are smooth, the direct and transmission waves are dominated in the common-shot-gathers (CSGs) [32]. To reduce the computation burden, the CSGs are down-sampled from  $n_z \times n_x = 5000 \times 200$  to  $200 \times 200$ .

We employ the Adam optimizer [33] to train the network with 50 epochs. The mean-square errors (MSE) and structural similarity indexes (SSIM) of the results are compared in Figure 7. We observe the results that the shallow parts of the velocity maps are inverted well for all the tests, but there are some mismatches between the predicted maps and true maps in the deep areas. This is because transmission waves dominate the seismic data since they have higher amplitudes than the reflection waves.

3) *High-resolution Inversion:* Another neural network is built to construct the high-frequency components. Similar to conventional FWI approaches, the result from the low-

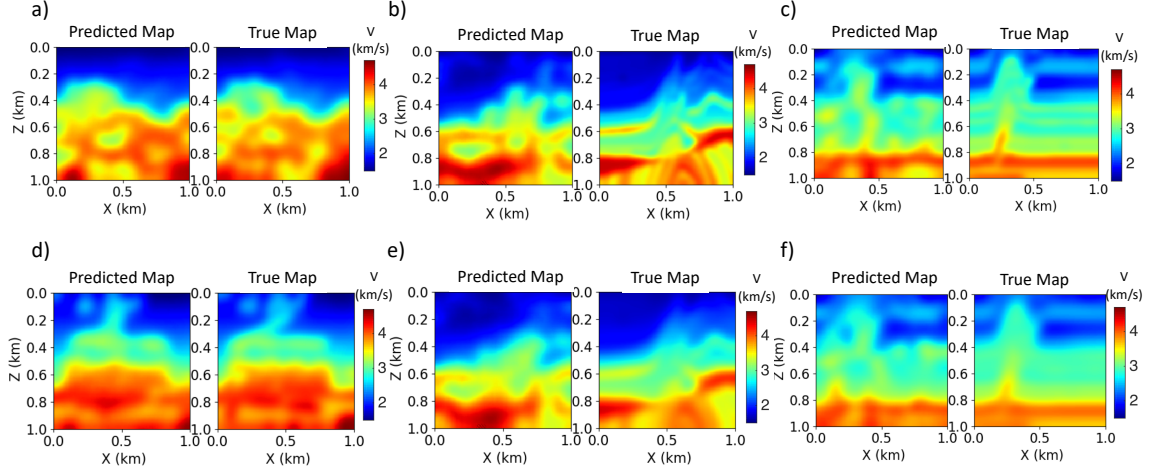


Fig. 7: a) and d) The predicted maps and true maps in the test set given by low-resolution InversionNet. b) and e) The predicted map and true Marmousi maps with different resolutions given by low-resolution InversionNet. c) and f) The predicted map and true Overthrust maps with different resolutions given by low-resolution InversionNet. The errors of the initial maps associated with a) to f) are (0.0212, 0.7820), (0.1065, 0.5266), (0.0343, 0.6374), (0.0138, 0.7846), (0.0720, 0.6397) and (0.0200, 0.7377), respectively. We report the error in the format of (MSE, SSIM).

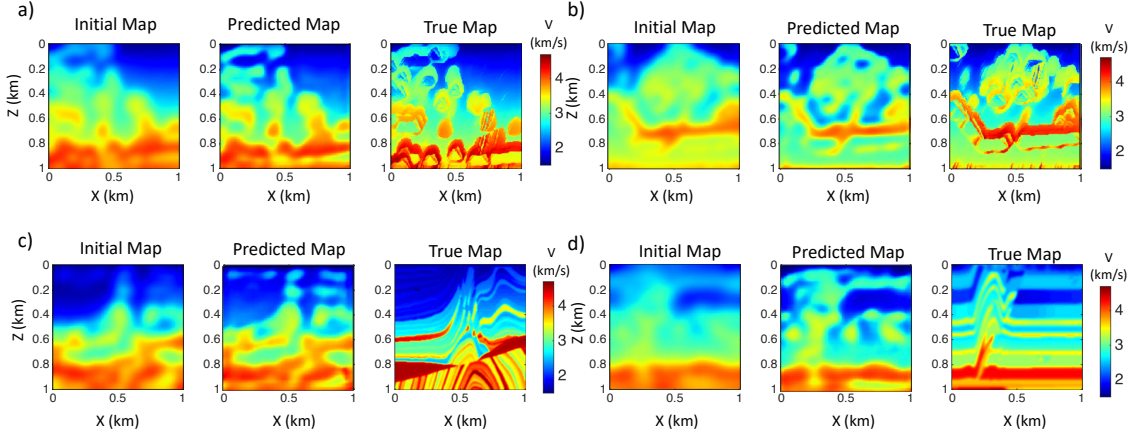


Fig. 8: a) and b) The initial maps, predicted maps and true maps in the test set and the initial maps, predicted maps and true maps with c) Mamoursi map and d) Overthrust map given by high-resolution InversionNet with  $\ell_2$  loss. The errors of the initial maps associated with a) to d) are (0.0650, 0.4867), (0.0741, 0.4938), (0.1821, 0.1693) and (0.0709, 0.3586), respectively. The errors of the predicted maps associated with a) to d) are (0.0361, 0.5394), (0.0501, 0.4950), (0.2281, 0.1522) and (0.1188, 0.2895), respectively. We report the error in the format of (MSE, SSIM).

resolution inversion is used as the initial guess. The data residual between the initial maps and the true maps is calculated. 64,000 groups of high-resolution velocity maps, initial guesses and their data residual are used for training with high-resolution InversionNet and another 3,000 groups are used for testing, respectively.

The high-resolution InversionNet is trained with  $\ell_2$  loss (Eq. (11)) and  $\ell_1$  loss (Eq. (12)). Accordingly, we provide the reconstruction results of these two strategies in Figures 8 and 9, respectively. We notice that the resolution of the velocity maps (particularly the one using the  $\ell_1$  loss) has been significantly improved from the low resolution results.

However, the small reflection events in the maps cannot affect the loss much since the loss function is based on the velocity maps. As a consequence, only the big reflection events can be inverted clearly while the small events cannot be seen. Particularly, for the Marmousi test data, the shallow parts are inverted well. However, the folds are inverted as anomalies in the shallow parts since there are no bending structures in our training set, these anomalies leads to an increase in the  $\ell_2$  loss of velocity maps. For the Overthrust test data, the reflectors at  $x = 0.2$  km and  $0.8$  km are inverted correctly. For the Overthrust data, the overthrust structures from  $x = 0.2$  km to  $0.5$  km are too complex so that the structure is strongly

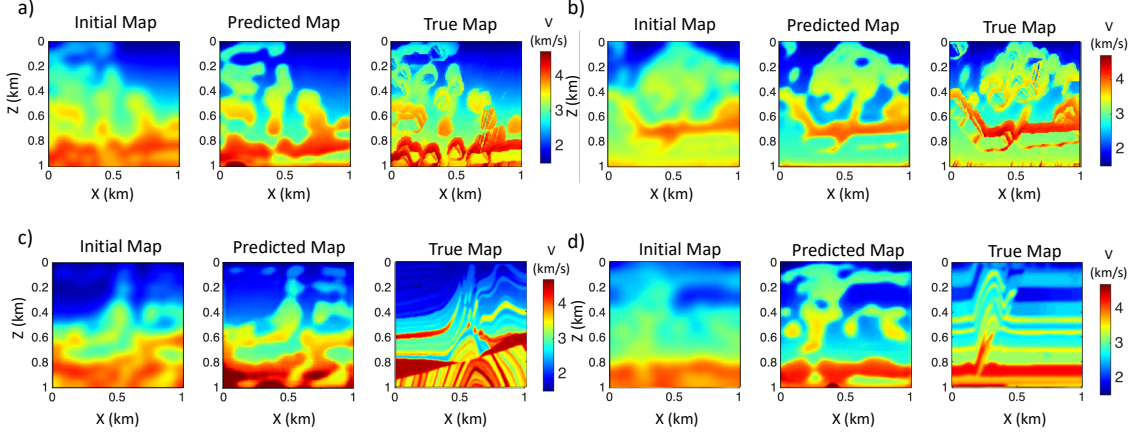


Fig. 9: a) and b) The initial maps, predicted maps and true maps in the test set and the initial maps, predicted maps and true maps with c) Marmousi map and d) Overthrust map given by high resolution InversionNet with  $\ell_1$  loss. The errors of the initial maps associated with a) to d) are (0.0650, 0.4867), (0.0741, 0.4938), (0.1821, 0.1693) and (0.0709, 0.3586), respectively. The errors of the predicted maps associated with a) to d) are (0.0453, 0.5484), (0.0512, 0.5139), (0.2538, 0.1430) and (0.1537, 0.2779), respectively. We report the error in the format of (MSE, SSIM).

distorted. Moreover, the thin flat reflectors from  $z = 0.4$  km to 0.8 km are not inverted correctly because of the lack of such kind of structures in the training set. We have simulated the seismic measurements using the initial maps and predicted maps from the high-resolution InversionNet as shown in Figure 10. The  $\ell_2$  loss of the seismic measurements decrease in the Marmousi test as the high-resolution InversionNet inverted the reflection waves. In the Overthrust test, both  $\ell_2$  loss of seismic measurements and velocity maps increase due to the distorted structures.

For comparison, we test InversionNet without the multiscale strategy on the same data, the corresponding results being shown in Figure 11. Without the constraint from the low-resolution InversionNet, the predicted velocity maps on the test data are inconsistent with the ground truth. The predicted velocity maps of the Marmousi test data and Overthrust test data are far from their ground truth. The MSE are higher and SSIM are lower than our Multiscale InversionNet results.

4) *Data-driven FWI vs Physics-based FWI*: We also provide numerical tests to compare the performance of physics-based FWI with data-driven FWI. The conventional and multiscale FWI tomograms [20] for Marmousi data are shown in Figure 12. We employ conjugated gradient method [34] to solve the conventional FWI. It is an iterative solver, which requires an initial guess to start with. We choose three different but commonly used initial guesses including a homogeneous velocity map (Figure 12(a)), a 1D linearly increasing velocity map (Figure 12(b)) and a smoothed Marmousi velocity map (Figure 12(c)). Observed from Figure 12(a), both conventional and multiscale FWI fails to yield reasonable results with the homogeneous velocity map as the initial guess. When the initial guess is 1D linearly increasing velocity map (Figure 12(b)), the conventional FWI quickly falls in local minimum after a few iterations, while the multiscale FWI can obtain reasonable results. For smoothed Marmousi velocity

map as initial guess, both conventional and multiscale FWI can achieve good results (shown in Figure 12(c)). Hence, the quality of the initial guess greatly impacts the inversion results when utilizing conventional FWI solvers. Many methods have been made to obtain good initial guesses, such as normal moveout (NMO) [35], dip moveout (DMO) [36], traveltimes tomography [21], migration velocity analysis [37], and many others. However, these methods have their own limitations, such as lack of low accuracy, limited illumination and high computation cost.

Compared to the physics-based FWI method, the data-driven FWI methods do not require an initial velocity map. It directly provides promising results regardless of prior initial guess information. It is worthwhile to mention that the low-resolution inversion results obtained using InversionNet can be also used as the initial guess for physics-driven FWI.

The computation times for the physics-based FWI methods running on a 18-core Intel Xeon computing node and the data-driven FWI methods running on a Tesla V100 GPU are given in Figure 13. For the training of each network and training data preparation, the computation time is 2 to 3 times greater than the physics-based FWI methods. Once network is fully trained, it can generate the inversion results almost instantaneously, and that is much more computationally efficient than the physics-based FWI methods.

## B. Field Data Test

1) *Training Data Preparation and Field Data Description*: Employing inversion algorithms on test data is challenging for both physics-based and data-driven inversion methods. In this section, we test our method on a 2D Gulf of Mexico (GOM) data set and compare it with two physics-based seismic inversion methods: the wave equation traveltimes tomography (WT) [38] and multiscale FWI. The initial model for the multiscale FWI is obtained by traveltimes tomography.



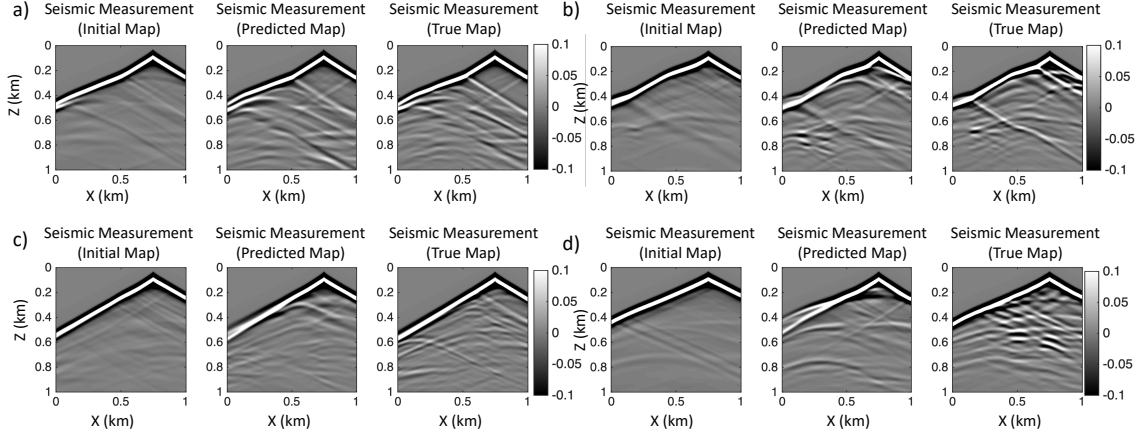


Fig. 10: a) and b) The seismic measurements simulated with the initial maps, predicted maps and true maps in the test set and the initial maps, predicted maps and true maps with c) Mamoursi map and d) Overthrust map given by high resolution InversionNet with  $\ell_1$ . The MSE errors of the initial maps associate with a) to d) are 0.0250, 0.2093, 0.1782 and 0.3877, respectively. The MSE errors of the predicted maps associate with a) to d) are 0.0210, 0.1021, 0.0505 and 0.4732, respectively.

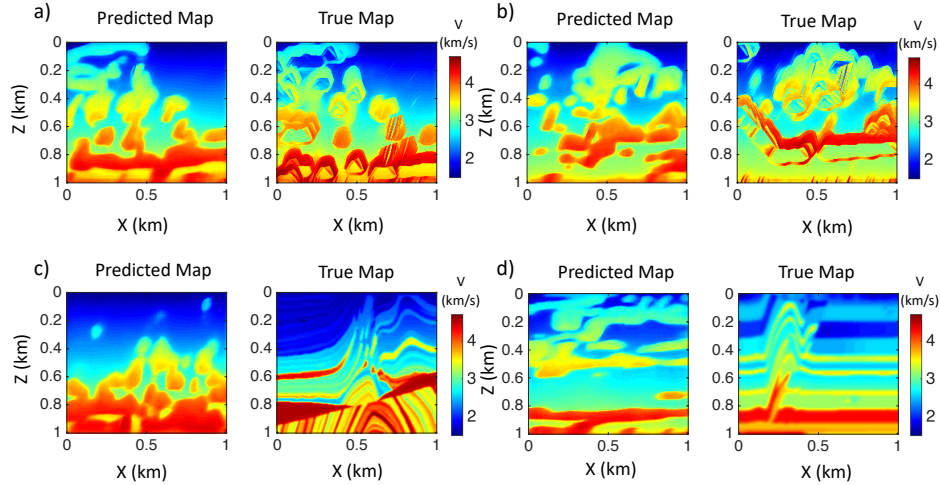


Fig. 11: a) and b) Predicted maps and true maps in the test set and predicted maps and true maps with c) Mamoursi map and d) Overthrust map given by InversionNet with  $\ell_2$  loss. The errors of the predicted maps associated with a) to d) are (0.0944, 0.3582), (0.1794, 0.2512), (0.2415, 0.0772) and (0.1737, 0.1317), respectively. We report the error in the format of (MSE, SSIM).

We use the same 67,000 realistic velocity maps with the synthetic tests except the size of the velocity maps are reshaped into 8.125 km in the  $x$  direction and 1.5 km in the  $z$  direction, with a grid spacing of 6.25 m. To make the survey configuration consistent with the field survey, 10 shot gathers are distributed on the surface of the map with a shot interval of 375 m, and each shot is recorded by a 6 km long cable with 480 receivers having a 12.5 m receiver interval. The shortest offset is 200 m. The source wavelet is extracted from the raw data by stacking the time-shifted reflection events together from 200 to 250 m offset in the shot gathers.

2) *Low-resolution Inversion:* To invert the low-frequency components of the velocity maps, we generate seismic data using 64,000 low-resolution velocity structures. The reflection

waves in the seismic measurements are muted, which means all the waves after the direct waves are removed [39]. Then the CSGs are downsampled to  $200 \times 200$  for training. An example of the muted field data is shown in Figure 14(a). We observe that the transmission waves are the main part and a small portion of reflection events remains in the data. The low resolution InversionNet has been trained for 10 epochs and then tested on the test data and GOM data.

Unlike tests using synthetic data, justifying the quality of inversion results from field data can be challenging in that it requires both qualitative tool and domain knowledge. In this work, we use reverse time migration (RTM) as a quality control (QC) tool to validate the inversion results, WT tomograms [21] and full-waveform tomograms [40]. RTM



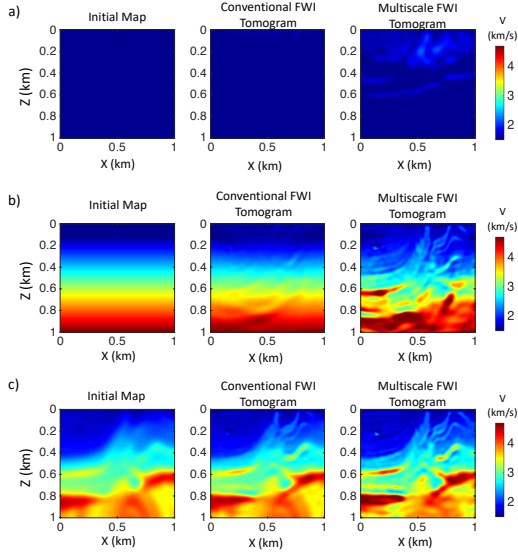


Fig. 12: a) A homogeneous map, b) a 1D linearly increasing map and c) a smoothed Marmousi map as the initial maps and their corresponding tomograms with conventional FWI and multiscale FWI. The errors of the initial maps associated with a) to c) are (4.1385, 0.0115), (0.3198, 0.0851) and (0.1168, 0.1017), respectively. The errors of the conventional FWI tomograms associated with a) to c) are (2.6499, 0.0092), (0.3018, 0.0559) and (0.0995, 0.1855), respectively. The errors of the multiscale FWI tomograms associated with a) to c) are (2.5565, 0.0306), (0.3292, 0.1177) and (0.0897, 0.2664), respectively. We report the error in the format of (MSE, SSIM).

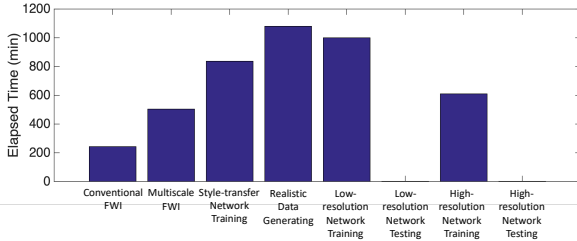


Fig. 13: Histogram comparison of computation times for the physics-based FWI and data-driven FWI methods.

is a seismic technique, which provides the visualization of the subsurface reflectivity using recorded seismic data. It is highly sensitivity to velocity errors, which result in a defocused and incoherent migration image [41]. Hence, RTM technique has been widely used as a quality-control (QC) tool in seismic imaging [42]. We provide the RTM images corresponding to different inversion results in Figure 15. The enlarged visualizations of the yellow and red boxes in the RTM images are shown in Figure 16. Since both WT inversion and low-resolution InversionNet inversion mainly focus on the transmission waves, the RTM images in 15(b) and 15(f) are comparable. However, there are a few reflection waves left in the muted data. Hence, the low-resolution InversionNet can invert and obtain the velocity structure in the deep region. As a result, the reflection events in the deep regions, such as the

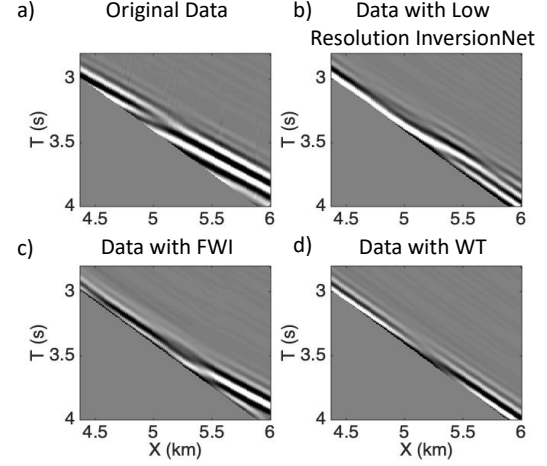


Fig. 14: a) Original data and data simulated with b) low resolution InversionNet result, c) FWI tomogram and d) WT tomogram.

reflection events which the yellow arrows point in Figure 16(c) is more focused and continuous than them in Figure 16(a).

In addition, we simulate transmission data with the predicted maps using WT and FWI tomograms as shown in the Figure 14. For comparison, these data are filtered by a 10 Hz low-pass filter. To better visualize the differences in data, we provide the traces in Figure 17. We observe that the data simulated from low-resolution InversionNet (Figure 17(a)) is in consistent with the original data. The data from FWI (Figure 17(b)) has a phase shift when comparing with the original data. For the data with WT (Figure 17(c)), the waveform does not match the original data since WT only considers the first arrival traveltimes.

3) *High-resolution Inversion*: For inverting the high-frequency component of the velocity map, we make use of the reflection waves to update the velocity map from low-resolution InversionNet. We mute all the waves before the direct waves and preserve reflection waves. After training for 5 epochs, we apply the high-resolution InversionNet on both the test data and GOM data. RTM is used as the QC tool since the velocity errors leads to defocused and discontinued RTM images [42]. The enlarged visualizations of the RTM images in these area are shown in Figure 16. Compared to the transmission waves, the illuminations of the reflection waves are deeper and wider. The boundary part of the velocity map from  $X = 5.5$  to  $7.2$  km can be updated by the high-resolution InversionNet. Since both FWI and high-resolution InversionNet take advantages of the reflection wave, the RTM image as pointed by the red arrows in Figure 16(b) and 16(d) are more continuous and focused than those in Figure 16(a) and 16(c), which only utilize transmission waves.

Then we compare the FWI tomograms and high-resolution result in Figure 15c and 15g. The velocity starts to increase around  $Z = 0.5$  km for both results, but the difference is that there is a low-velocity zone from  $X = 3$  to  $5$  km in the high-resolution InversionNet results. As a result, the enlarged visualizations of the RTM images in Figure 16(f) and 16(h)

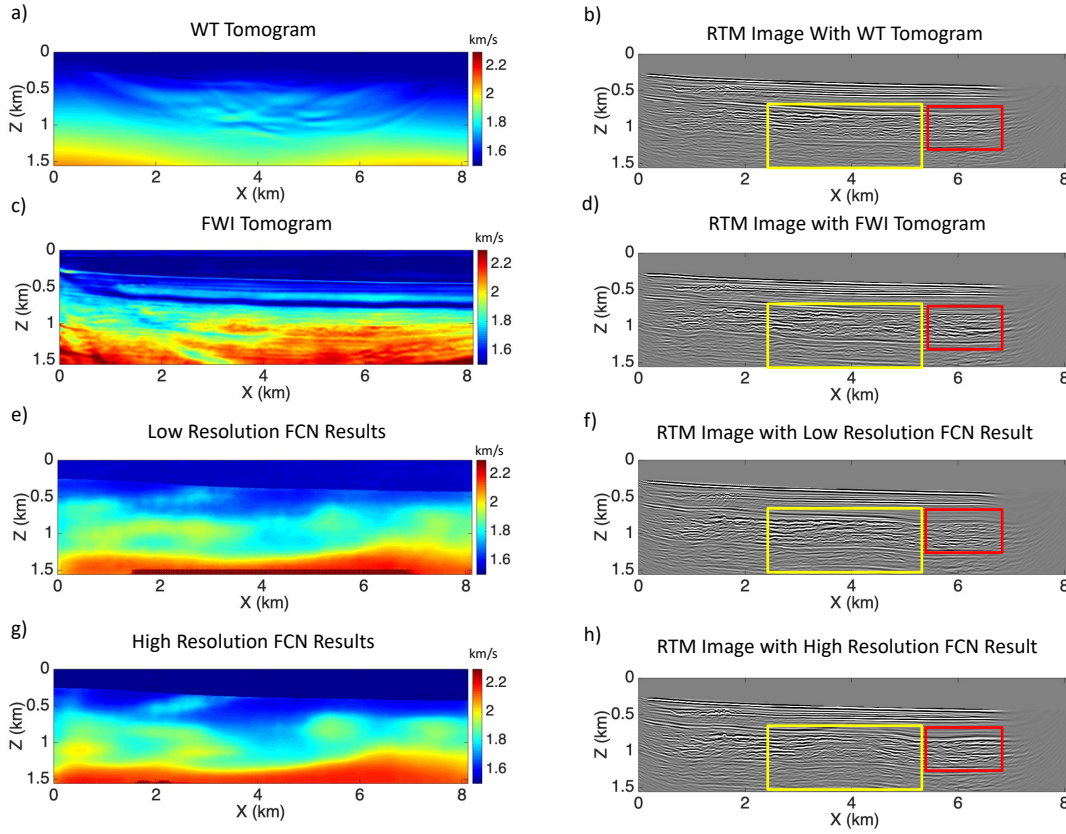


Fig. 15: a) and b) WT tomogram and its RTM image. c) and d) FWI tomogram and its RTM image. e) and f) Low Resolution InversionNet result and its RTM image. g) and h) High Resolution InversionNet result and its RTM image.

are different. But both of them are continuous, so it is hard to judge which one is better. Moreover, it is hard to tell why there is such a big difference since the network is a black box.

## V. DISCUSSION AND FUTURE WORK

### A. “Doing More with Less”—Incorporating Physics in Scientific Machine Learning

Domain-aware learning is a unique and critical task to scientific machine learning (SciML) [43]. Our work explores particular avenues of incorporating critical physics knowledge in SciML through the problem of computational imaging. Labeled real data is extremely valuable but also costly to obtain in scientific applications. Our approach provides a feasible and cost-effective solution to address the dilemma of data scarcity for deep learning approaches. Built on style-transfer approaches, we develop a method to synthesize physically realistic subsurface structure images that can be used to augment the training set and enrich the representativeness of the data. Our approach has significant potential in that it not only leverages the existing large volume of natural images with diversified representation, but also accounts for critical physics and domain knowledge.

Many scientific problems involve systems that are governed by complex physical laws. It has recently been shown in the literature that there is a benefit to accounting for those physics in the design of the neural networks [16]. We propose and

develop a particular strategy to decouple complex physics phenomena into simple ones, which can be separately incorporated into neural networks. Comparing to those end-to-end strategy of incorporating domain knowledge, our mean of multiscale data-driven method better leverages the physics information, which results in significantly improved imaging results with much higher resolution.

### B. Scientific “Sim2Real”

Physical simulation is an important tool for scientific problems. Originated in the robotics and vision community, the concept of “Sim2Real” refers to the ideas of transferring knowledge learned in simulation to the real data [44]. Due to the lack of real labeled data in subsurface geophysics, model-based simulators have been widely used to synthesize simulations. However, pure model-based simulators usually simplifies the complex physics systems, which result in unavoidable reality gap between the simulation and real data. This gap degrades the predictivity and generalization ability of a predictive model. Our approach, on the other hand, is model-free and it learns the heuristic physics implicitly through the data without explicitly imposing physics rules. We demonstrate its capability in learning the physics to generate physically realistic data for training predictive model. We further apply our predictive model to both out-of-distribution synthetic test data and real test data set. The results obtained are promising, which in turn proves the effectiveness of our approach in

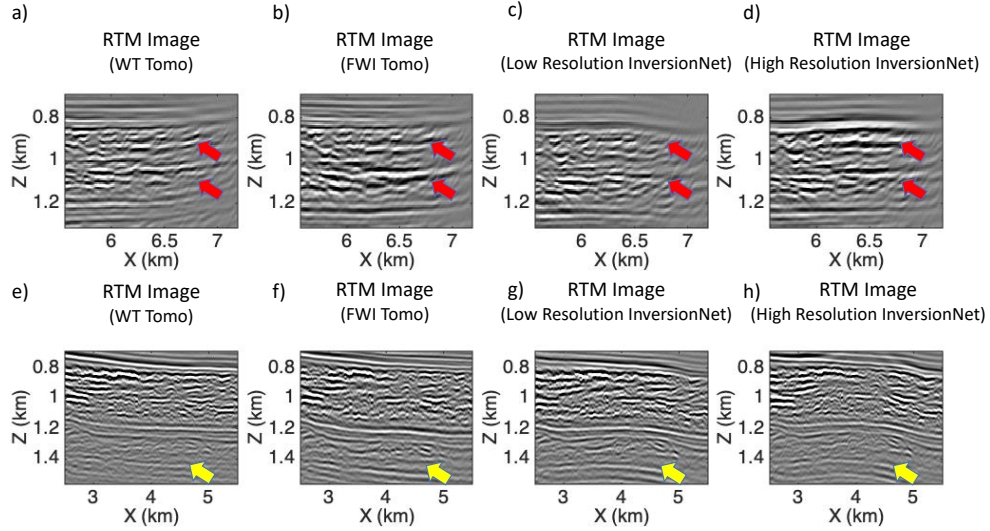


Fig. 16: The enlarged visualization of the RTM images in red boxes (Row 1) and yellow boxes (Row 2) in Figures 15(b), 15(d), 15(f) and 15(h).

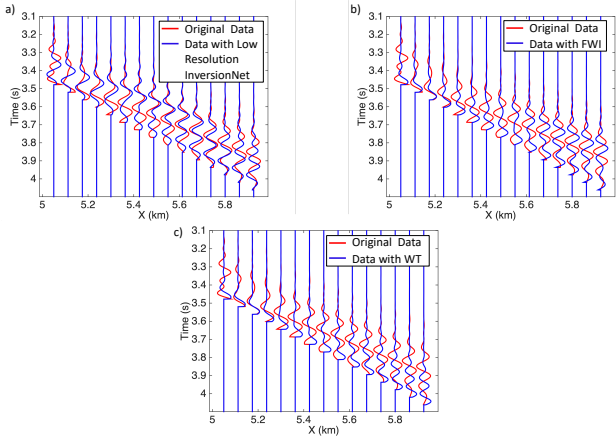


Fig. 17: Wiggle trace comparison between original data and data simulated with a) low resolution InversionNet result, b) FWI tomogram and c) WT tomogram.

synthesizing simulation. However, there are still artifacts and missing information in the inversion results observable when applying our data-driven techniques to the Overthrust data set (as shown in Figures 8 and 9). To further improve the inversion, a more diversified training set would be needed to capture various kinds of subsurface geology structures. One potential approach to increase the representativeness of our training set is to incorporate multiple subsurface style maps with orthogonal features (meaning styles represented by different geology images do not overlap).

### C. Computational Benefits and Broader Applicability

Our work is to address two important challenges in data-driven computational seismic imaging: accuracy and efficiency. As shown in our numerical tests, our data-driven inversion method outperforms the conventional FWI methods by alleviating several major computational issues such as local

minima and need of good initial guess. We also show that once fully trained, our data-driven inversion model can be significantly more efficient in inferring subsurface structure than the conventional seismic imaging techniques. We demonstrate the efficacy of our model using both synthetic and field data. To the best of our knowledge, this is the first work to employ data-driven full-waveform inversion method in characterizing a complex field data rather than simple layer-based structure.

Similar computational challenges exist among many computational imaging problems including seismic imaging. Although we demonstrate the performance of our new techniques using computational seismic imaging problem, our methods are not restricted to this particular application. It can be potentially applicable to much broad computational imaging problems such as medical ultrasound tomography, radar imaging, microscope imaging, and many others.

### D. Future Work

Different approaches have been used in decoupling the complex wave phenomena. Our approach is one of the many. It would be worthwhile to explore the benefits of other means in decoupling complex waves. An example of this would be the frequency decomposition, where a wave is decomposed into different frequency bands [45]. However, our network structure is designed to be technically flexible in incorporating of different decomposition of wave physics.

Loss function plays an important role in obtaining a predictive model. Throughout this work, we employ loss function on the subsurface velocity domain to justify the correctness of the inversion model. Our tests show that, that once converged, the training accuracy of our model can reach as high as 95%, which leads to a successful reconstruction of the major subsurface structures through training. However, it is the last 5% of the training error that would contribute to further refining the subsurface structures with more details. This issue is essentially caused by the fact that our loss function is lack of

data consistency. Similar problems have been also identified in other computational imaging applications [46]. One potential approach to compensate for missing details would be a cycle-consistency loss [47], which takes the advantage of both the image loss as well as the data loss. This is one of our future direction.

Physics-based regularization techniques have been proved useful in improving resulting inversion for conventional FWI approaches. One example of those would be the illumination compensation, which have been usually used in conventional FWI methods to regularize the inversion and help with the deep regions [48]. However, in our current model we have not yet employ any physics-based regularization to constrain our results. One of our future direction would be applying illumination regularization in the data domain along the  $z$  direction for increasing the prediction accuracy.

## VI. CONCLUSIONS

In this paper, we develop a multiscale data-driven seismic imaging technique. The inversion procedure has been separated into two steps that invert for low-frequency and high-frequency components of the velocity maps, respectively. In particular, we design two different neural networks to account for different wave phenomena. To focus on the direct and transmission waves, we design the first network based on InversioNet and train it with smoothed velocity and their corresponding seismic measurements. To take the advantage of the reflection wave and refine the inversion results obtained from the first neural network, we further design and train the second neural network using high-resolution velocity maps, the inversion results generated with the previous network and their data residuals. A high quality training set is the foundation for an effective data-driven inversion approach. We develop a technique to generate physically meaningful subsurface velocity maps with sufficient variability. Our technique is developed based on style transfer method that is capable of transferring a large amount of natural images to realistic subsurface velocity maps. To validate the performance of our synthesized training set and the data-driven inversion techniques, we compare our approaches to conventional physics-based seismic imaging methods using both the synthetic and field data sets. Our results show that once fully trained using properly designed training set, our data-driven inversion model is much more efficient than those physics-based inversion methods and yields significantly improved imaging results.

## ACKNOWLEDGEMENTS

This work was co-funded by the U.S. DOE Office of Fossil Energy's Carbon Storage program and by the Laboratory Directed Research and Development program of LANL under project numbers 20210542MFR and 20200061DR.

## REFERENCES

- [1] A. Tarantola, *Inverse problem theory and methods for model parameter estimation*. SIAM, 2005.
- [2] J. Virieux and S. Operto, "An overview of full-waveform inversion in exploration geophysics," *Geophysics*, vol. 74, no. 6, pp. WCC1–WCC26, 2009.
- [3] A. Poole, P. Bilsby, and G. Busanello, "The five v's of big seismic data," *80th EAGE Conference and Exhibition*, vol. 2018, no. 1, pp. 1–5, 2018.
- [4] Y. Wu and Y. Lin, "InversionNet: An efficient and accurate data-driven full waveform inversion," *IEEE Transactions on Computational Imaging*, vol. 6, no. 1, pp. 419–433, 2019.
- [5] S. Li, B. Liu, Y. Ren, Y. Chen, S. Yang, Y. Wang, and P. Jiang, "Deep learning inversion of seismic data," *arXiv preprint arXiv:1901.07733*, 2019.
- [6] F. Yang and J. Ma, "Deep-learning inversion: A next-generation seismic velocity model building method," *Geophysics*, vol. 84, no. 4, pp. R583–R599, 2019.
- [7] Z. Zhang and Y. Lin, "Data-driven seismic waveform inversion: A study on the robustness and generalization," *IEEE Transactions on Geoscience and Remote Sensing*, vol. 58, no. 10, pp. 6900–6913, 2020.
- [8] R. Rojas-Gomez, J. Yang, Y. Lin, J. Theiler, and B. Wohlberg, "Physics-consistent data-driven waveform inversion with adaptive data augmentation," *IEEE Geoscience and Remote Sensing Letters*, 2020.
- [9] J. Sun, Z. Niu, K. A. Innanen, J. Li, and D. O. Trad, "A theory-guided deep-learning formulation and optimization of seismic waveform inversion," *Geophysics*, vol. 85, pp. 1MA–Z8, 2020.
- [10] E. Schat, R. Schoot, W. M. Kouw, D. Veen, and A. M. Mendrik, "The data representativeness criterion: Predicting the performance of supervised classification based on data set similarity," *PLoS ONE*, vol. 15, no. 8, p. e0237009, 2020.
- [11] O. Ovcharenko, V. Kazei, D. Peter, and T. Alkhalifah, "Style transfer for generation of realistically textured subsurface models," in *SEG Technical Program Expanded Abstracts 2019*. Society of Exploration Geophysicists, 2019, pp. 2393–2397.
- [12] X. Wu, Z. Geng, Y. Shi, N. Pham, S. Fomel, and G. Caumon, "Building realistic structure models to train convolutional neural networks for seismic structural interpretation," *Geophysics*, vol. 85, no. 4, pp. WA27–WA39, 2020.
- [13] J. Johnson, A. Alahi, and L. Fei-Fei, "Perceptual losses for real-time style transfer and super-resolution," in *European conference on computer vision*. Springer, 2016, pp. 694–711.
- [14] L. A. Gatys, A. S. Ecker, and M. Bethge, "A neural algorithm of artistic style," *arXiv preprint arXiv:1508.06576*, 2015.
- [15] —, "Image style transfer using convolutional neural networks," in *Proceedings of the IEEE conference on computer vision and pattern recognition*, 2016, pp. 2414–2423.
- [16] M. Raissi, P. Perdikaris, and G. Karniadakis, "Physics-informed neural networks: A deep learning framework for solving forward and inverse problems involving nonlinear partial differential equations," *Journal of Compu-*



- tational Physics*, vol. 378, pp. 686–707, 2019.
- [17] M. Raissi, P. Perdikaris, and G. E. Karniadakis, “Physics informed deep learning (part i): Data-driven solutions of nonlinear partial differential equations,” *arXiv preprint arXiv:1711.10561*, 2017.
  - [18] —, “Physics informed deep learning (part ii): Data-driven discovery of nonlinear partial differential equations,” *arXiv preprint arXiv:1711.10566*, 2017.
  - [19] W. Wang and J. Ma, “Velocity model building in a cross-well acquisition geometry with image-trained artificial neural networks,” *Geophysics*, vol. 85, no. 2, pp. U31–U46, 2020.
  - [20] C. Bunks, F. M. Saleck, S. Zaleski, and G. Chavent, “Multiscale seismic waveform inversion,” *Geophysics*, vol. 60, no. 5, pp. 1457–1473, 1995.
  - [21] S. Feng and G. T. Schuster, “Transmission+ reflection anisotropic wave-equation traveltime and waveform inversion,” *Geophysical Prospecting*, vol. 67, no. 2, pp. 423–442, 2019.
  - [22] Z. Liu and L. Huang, “Multiscale and layer-stripping wave-equation dispersion inversion of rayleigh waves,” *Geophysical Journal International*, vol. 218, no. 3, pp. 1807–1821, 2019.
  - [23] T.-Y. Lin, M. Maire, S. Belongie, J. Hays, P. Perona, D. Ramanan, P. Dollár, and C. L. Zitnick, “Microsoft COCO: Common objects in context,” in *European conference on computer vision*. Springer, 2014, pp. 740–755.
  - [24] K. Simonyan and A. Zisserman, “Very deep convolutional networks for large-scale image recognition,” in *Proceedings of the International Conference on Learning Representations*, 2015.
  - [25] O. Ronneberger, P. Fischer, and T. Brox, “U-Net: Convolutional networks for biomedical image segmentation,” in *Medical Image Computing and Computer-Assisted Intervention (MICCAI)*, ser. LNCS, vol. 9351. Springer, 2015, pp. 234–241, (available on arXiv:1505.04597 [cs.CV]). [Online]. Available: <http://lmb.informatik.uni-freiburg.de/Publications/2015/RFB15a>
  - [26] A. Brougois, M. Bourget, P. Lailly, M. Poulet, P. Ricarte, and R. Versteeg, “Marmousi, model and data,” in *EAEG workshop-practical aspects of seismic data inversion*. European Association of Geoscientists & Engineers, 1990, pp. cp–108.
  - [27] R. J. Versteeg, “Sensitivity of prestack depth migration to the velocity model,” *Geophysics*, vol. 58, no. 6, pp. 873–882, 1993.
  - [28] Y. Wang, “Frequencies of the ricker wavelet,” *Geophysics*, vol. 80, no. 2, pp. A31–A37, 2015.
  - [29] A. Fichtner, *Full seismic waveform modelling and inversion*. Springer Science & Business Media, 2010.
  - [30] R. Alford, K. Kelly, and D. M. Boore, “Accuracy of finite-difference modeling of the acoustic wave equation,” *Geophysics*, vol. 39, no. 6, pp. 834–842, 1974.
  - [31] F. Aminzadeh, N. Burkhard, J. Long, T. Kunz, and P. Duclos, “Three dimensional seg/eaeg models—an update,” *The Leading Edge*, vol. 15, no. 2, pp. 131–134, 1996.
  - [32] M. Reshef and D. Kosloff, “Migration of common-shot gathers,” *Geophysics*, vol. 51, no. 2, pp. 324–331, 1986.
  - [33] D. P. Kingma and J. Ba, “Adam: A method for stochastic optimization,” *arXiv preprint arXiv:1412.6980*, 2014.
  - [34] M. J. D. Powell, “Restart procedures for the conjugate gradient method,” *Mathematical programming*, vol. 12, no. 1, pp. 241–254, 1977.
  - [35] S. Feng, O. Yilmaz, Y. Chen, and G. T. Schuster, “Zero-offset sections with a deblurring filter in the time domain,” *Geophysics*, vol. 84, no. 4, pp. S239–S249, 2019.
  - [36] D. Hale, “Dip-moveout by fourier transform,” *Geophysics*, vol. 49, no. 6, pp. 741–757, 1984.
  - [37] Z. Feng, B. Guo, and L. Huang, “Joint pp and ps plane-wave wave-equation migration-velocity analysis,” *Geophysics*, vol. 84, no. 4, pp. R507–R525, 2019.
  - [38] Y. Luo and G. T. Schuster, “Wave-equation traveltime inversion,” *Geophysics*, vol. 56, no. 5, pp. 645–653, 1991.
  - [39] Ö. Yilmaz, *Seismic data analysis: Processing, inversion, and interpretation of seismic data*. Society of exploration geophysicists, 2001.
  - [40] Y. Huang and G. T. Schuster, “Full-waveform inversion with multisource frequency selection of marine streamer data,” *Geophysical Prospecting*, vol. 66, no. 7, pp. 1243–1257, 2018.
  - [41] J. Yang, Y. Elita Li, A. Cheng, Y. Liu, and L. Dong, “Least-squares reverse time migration in the presence of velocity errors,” *Geophysics*, vol. 84, no. 6, pp. S567–S580, 2019.
  - [42] G. Shan, L. Zhang, Y. Wang, T. Nemeth, and W. Liu, “Velocity sensitivity of reverse-time migration,” in *SEG Technical Program Expanded Abstracts 2008*. Society of Exploration Geophysicists, 2008, pp. 2321–2325.
  - [43] “Basic research needs for scientific machine learning,” U.S. the Department of Energy Advanced Scientific Computing Research, Tech. Rep., 2019.
  - [44] S. James, P. Wohlhart, M. Kalakrishnan, D. Kalashnikov, A. Irpan, J. Ibarz, S. Levine, R. Hadsell, and K. Bousmalis, “Sim-to-real via sim-to-sim: Data-efficient robotic grasping viarandomized-to-canonical adaptation networks,” in *IEEE International Conference on Computer Vision*, 2019.
  - [45] C. Bunks, F. M. Saleck, and S. Zaleski, “Multiscale seismic waveform inversion,” *Geophysics*, vol. 60, no. 5, p. 1457–1473, 1995.
  - [46] D. Otero, J. Leuschner, and M. Schmidt, “Computed tomography reconstruction using deep image prior and learned reconstruction methods,” *arXiv preprint arXiv:2003.04989*, 2020.
  - [47] J. Zhu, T. Park, P. Isola, and A. Efros, “Unpaired image-to-image translation using cycle-consistent adversarial networks,” in *IEEE International Conference on Computer Vision*, 2017.
  - [48] J. E. Rickett, “Illumination-based normalization for wave-equation depth migration,” *Geophysics*, vol. 68, no. 4, pp. 1371–1379, 2003.